RESEARCH ARTICLE | OCTOBER 11 2023

A multiscale 3D hotspot-rich nanostructured substrate for biomolecular detection of SARS-CoV-2

Smruti R. Sahoo ; Chun-Ta Huang ; Kunju Tsai ; Gou-Jen Wang ; Cheng-Chung Chang

Appl. Phys. Rev. 10, 041403 (2023)
https://doi.org/10.1063/5.0155256

Applied Physics Reviews ARTICLE pubs.aip.org/aip/are

A multiscale 3D hotspot-rich nanostructured substrate for biomolecular detection of SARS-CoV-2

Cite as: Appl. Phys. Rev. **10**, 041403 (2023); doi: 10.1063/5.0155256
Submitted: 19 April 2023 · Accepted: 22 September 2023 ·
Published Online: 11 October 2023

View Online Export Citation CrossMark

Smruti R. Sahoo,[1,2] Chun-Ta Huang,[3] Kunju Tsai,[4] Gou-Jen Wang,[2,5,a)] and Cheng-Chung Chang[1,5,a)]

AFFILIATIONS

[1]Intelligent Minimally-Invasive Device Center, National Chung Hsing University, Taichung 402, Taiwan
[2]Department of Mechanical Engineering, National Chung-Hsing University, Taichung 40227, Taiwan
[3]Protrustech Co., Ltd., 3F.-1, No. 293, Sec. 3, Dongmen Rd. East District, Tainan City 701, Taiwan
[4]Nanovie Co., Ltd., Taichung 41107, Taiwan
[5]Graduate Institute of Biomedical Engineering, National Chung Hsing University, Taichung 402, Taiwan

Note: This paper is part of the APR Special Topic on Materials and Technologies for Bioimaging and Biosensing.
[a)]**Authors to whom correspondence should be addressed:** gjwang@dragon.nchu.edu.tw and ccchang555@dragon.nchu.edu.tw

ABSTRACT

The current fabrication methods of surface-enhanced Raman scattering (SERS) chips used for biological detection mostly require antibodies conjugated on nanostructured metals or additionally connected to a reporter, which leads to complicated fabrication processes and increases the cost of these chips. More importantly, only a single-layer (2D) signal source is generated on the substrate of the chip, resulting in poor sensitivity. Herein, we constructed a single-component, multiscale, three-dimensional SERS (M3D-SERS) substrate from silver nanowires (AgNWs) packing. According to our results, the Raman enhancement effect of the M3D-SERS substrate was related to the degree of AgNWs stacking along the z axis. In addition, the light source-dependent plasmonic partition and hotspot formation of the M3D-SERS substrate were evaluated by the finite integration technique to prove that M3D-SERS offers advantages, with isotropic localized surface plasmon resonance as well as homogeneous hotspot distribution, for SERS over its 1D and 2D counterparts. Experimentally, the optimal construction of the M3D-SERS chip was explored and established based on the Raman signal enhancement of bovine serum albumin, and consequently, the efficiency of the M3D-SERS chip in detecting SARS-CoV-2-related biomolecules was investigated based on the detection superiority to biomolecules. This study demonstrates a simple, label-free, pre-treatment-free potential biosensor technology that can be used in healthcare units. Furthermore, in combination with a suitable laser light source, this technology can be applied for efficient detection in point-of-care tests with a handheld spectrometer.

I. INTRODUCTION

The ease of synthesis methods and the fine control over nanostructured materials allow the study of light–matter interactions and the manipulation of light at the nanoscale in a well-controlled manner.[1] This has ushered in a field, plasmonics, which has played a dominant role in the enhancement of the small Raman-scattering cross sections of various molecules and substances. The extremely large electromagnetic fields from the localized plasmons at the surface of noble metal nanostructures are utilized to enhance the weakly scattered Raman signals from probe molecules, known as surface-enhanced Raman scattering (SERS). With SERS, it has been possible to achieve sensitivity down to the single-molecule level.[2,3] SERS was first observed with roughened substrates[4] and later with substrates decorated with nanoparticles (NPs) with different geometries and morphologies. The development of wet-chemical synthesis methods offered good control over the morphology of various types of nanostructures with different shapes and sizes, along with surface functionalization and tailored optical properties, in a highly reproducible manner.[5] This renders SERS a nondestructive technique with a wide application range, including food safety and clinical diagnosis.[6] Moreover, SERS substrates have many other additional advantages that enable them to be applicable under different environmental, analyte, or lasing conditions.

Therefore, based on the issue at hand, a suitable selection can be made regarding the substrate, required nanostructured material, and synthesis method. Owing to their unique dielectric properties, noble metal nanostructures of gold (Au) or silver (Ag) are specifically chosen as SERS substrates. In contrast to symmetric nanoparticles, such as nanospheres, anisotropic nanoparticles have larger SERS enhancement factors, owing particularly to the presence of edges, vertices, corners, or any sharp features, which serve as inherent hotspots.[7] Furthermore, the modification of nanostructures, such as chemical etching, coating with different materials, alignment, and geometries, is often performed to enhance the weakly scattered Raman signal. Quasi-one-dimensional nanostructures, such as nanowires (NWs) and nanorods, have excellent localized surface plasmon resonance (LSPR) tunability over the visible and near-infrared ranges, in addition to other advantages, such as acting as waveguides below the diffraction limit.[8]

Both label-free and Raman reporter-based indirect SERS studies have been conducted in regard to biomolecules, food and agricultural products, and clinical diagnosis.[9–18] The development of nanoparticle synthesis and fabrication technologies has resulted in the fabrication of a wide variety of SERS substrates, such as electrospun nanofibers,[19] silver-capped aluminum nanorods,[20] polystyrene (PS)/Cu_2S/Ag structures,[21] boron nitride (BN)-modified nanorod arrays,[22] TiO_2 nanorods decorated with gold nanoparticles,[23] Au–Ag bimetallic nanoparticles decorated silicon nanowires,[24] Ag/TiO_2 nanocomposites,[25] and Ag@ZnO@Bi_2WO_6 membrane disks,[26] to name a few. However, most of these substrates require rather complex fabrication processes and involve two or more materials with further pre/post-modification, and SERS substrates are limited to only one- or two-dimensional (1D/2D) structures.

In an attempt to overcome these issues, three-dimensional (3D)-structured SERS substrates have recently been developed. 3D structures provide a greater number of hotspots, with a large specific area for exposure to laser sources and probe molecules, and more importantly allow SERS enhancements to be engineered with a high degree of flexibility. Efforts are being focused on creating multilayer-structured nanoparticles, with the aim of improving the organization of the nanoparticles, which can yield more uniform distributions of hotspots.[7] By using 3D assemblies of plasmonic nanoparticles, Mueller *et al.*[27] achieved a uniformly enhanced SERS response, which was also well supported by finite-difference time domain (FDTD) simulations. Vieira *et al.* studied the plasmonic properties of both silver and gold nanoparticles in mono- and bilayer arrangements.[28] With the combined use of transmission electron microscopy (TEM), small-angle x-ray scattering (SAXS), and x-ray cross-correlation analysis (XCCA), Schulz *et al.*[29] studied the changes in the lattice constant and degrees of orientational order with an increase in the number of AuNP (gold nanoparticle) layers.[30] Zhou *et al.* demonstrated that selected R6G peak intensities follow an increasing trend toward an optimum value with an increase in Ag thickness and a reverse trend with a subsequent further increase in Ag thickness.[31] Despite all these advances in SERS with multilayered structures, such enhancements in single-component anisotropic noble metallic nanoparticle assemblies along with a combined theoretical approach for understanding the underlying mechanisms remain unexplored.

As COVID-19 has evolved into influenza, the high-cost and long-time detection of RT-PCR generation is over. Rapid screening became urgently needed. There must be a fast and accurate method to detect antibodies instead of viruses. Therefore, if there is a convenient detection method that can collect a strong signal, there is no need to use artificial intelligence enhancement, statistics, or other identification methods to increase the detection cost and time. To build an efficient biomolecule-detecting platform, we report a simple and economical method for fabricating a *single-component, multiscale/multilayer* chip, a three-dimensional surface-enhanced Raman scattering (M3D-SERS) substrate, from silver nanowires (AgNWs) without any pre- or post-modification. With regard to plasmon resonance, this kind of multilayer packing and its influence on electromagnetic field (E-field) generation remains unexplored to the best of our knowledge. Hence, we used computationally extensive electrodynamic simulations, via the finite integration technique (FIT), to investigate how such multilayer nanostructures influence SERS enhancements in M3D-SERS chips under different conditions. The effects of the length, diameter, interwire gaps, end-to-end gaps, intersecting nanowires, and layer dependence of the local electromagnetic field distributions were simulated to compare them with the corresponding experimental SERS results. We observed that the plasmonic properties of AgNWs were closely related to the morphological dimensions. Moreover, the multilayered structure of the 3D AgNW packing substrates caused *isotropic* plasmon enhancement based on the 3D *homogeneous* hotspot distribution. (Fig. 1) Experimentally, we collected the SERS signal criteria of the blank biomolecule bovine serum albumin (BSA) to explore the optimal layer packing of M3D-SERS, and this benchmark was not only used to doubly confirm the FIT theoretical calculations but also applied to perform SERS evaluation for other biomolecules. Consequently, from the perspective of attaining an effective fast-screening technique for the detection of SARS-CoV-2-related biomolecules, we present the efficiency of such a M3D-SERS chip in detecting SARS-CoV-2 S-protein and antibodies.

II. EXPERIMENTAL

A polyol method was adopted for the synthesis of AgNWs.[32,33] Materials used in the synthesis procedures and characterization techniques are described in detail in the electronic supplementary material (ESI).

A. Electromagnetic field simulations

The finite integration technique (FIT),[34] which allows discretized Maxwell's equations to be solved in an integral form, was used for E-field simulations of the nanostructures by CST Studio Suite. The dimensions of the AgNWs for the input simulation parameters were 5 μm (length) × 100 nm (diameter). Each AgNW was discretized by tetrahedral meshes, with fixed edge lengths of 1/5 of the radius of a AgNW. The solver accuracy of the equation system was set to 10^{-6}. All other contributing factors, such as higher orders of partial waves and retardation effects, were inherently considered for the simulations. The maximum E-fields from the AgNWs in different configurations under different laser excitation wavelength sources were expressed in terms of E^2. The dielectric permittivity of silver for the simulations was referenced from Johnson and Christy.[35]

B. Construction of a three-dimensional surface-enhanced Raman scattering (M3D-SERS) substrate

We adopted a layer-by-layer approach to construct a multilayer, three-dimensional SERS (M3D-SERS) substrate by using our as-synthesized silver nanowires in ESI. This as-synthesized silver nanowires with UV–Vis spectrophotometric optical density of

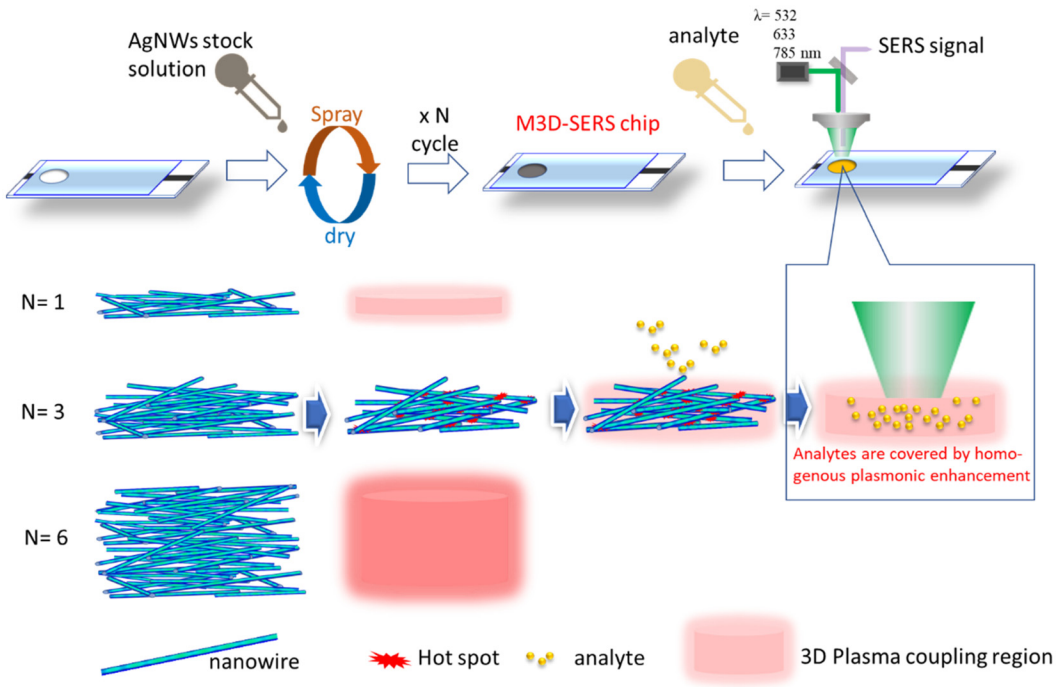

FIG. 1. Construction of multilayers following the layer-by-layer method: As-synthesized AgNWs were spread onto a glass substrate followed by vacuum drying (referred to as the first layer, 1 L). Likewise, the subsequent layers deposited as such after vacuum drying were labeled 2 L, 3 L, 4 L, 5 L, and 6 L.

2.6 (4.5 mg/mL) served as the stock solution for the fabrication of all the layered SERS substrates. A circular well on a glass plate with a diameter of 0.5 cm and depth of 0.02 cm is the substrate template. In a typical fabrication procedure, as shown in Fig. 1, the first layer was created by spraying 10 μL of the stock solution (with a handheld pipette positioned at a 45° angle) onto a circular well on the glass substrate. The AgNW structured first-layer substrate was then vacuum dried and stored in a vacuum desiccator to avoid any contamination from the external environment. After the substrate was fully dried, we labeled it layer 1 (1 L). Following the same approach, we sprayed another volume of the AgNWs (10 μL) stock solution onto the previously prepared 1 L substrates, and thus fabricated 2 L substrates, after vacuum drying. Therefore, these 2 L substrates contained a total of amount of 20 μL AgNWs. To construct a third-layer SERS substrate, the same constant volume (10 μL) of AgNWs was sprayed onto the 2 L substrate and vacuum dried. Consequently, this process was repeated for the construction of the fourth (4 L), fifth (5 L), and sixth (6 L) layered SERS substrates (M3D-SERS). A constant volume (10 μL) of target molecules, bovine serum albumin (BSA) and SARS-CoV-2-related biomolecules (antigens/antibodies), were used in this study. These target molecules were introduced into the multilayered AgNWs, followed by vacuum drying. In this way, the M3D-SERS substrate for drop casting the analyte-containing aqueous solution and drying was ready for SERS detection.

C. Characterization and SERS measurements

The surface morphology of the as-synthesized AgNWs was characterized by scanning electron microscopy (JEOL JSM-7800F Prime Schottky field emission scanning electron microscope). The optical absorbance of the AgNWs was measured by a Thermo Genesys 6 UV-visible spectrophotometer. Nano size measurement was performed by dynamic light scattering (DLS) using a SZ-100—HORIBA (Minami-ku Kyoto, Japan). A Thermo Scientific x-ray Photoelectron Spectrometer (XPS) with monochromatic Al K_α x-ray radiation at 1486.6 eV was employed to characterize the core energy levels of the 1 L–6 L SERS substrates. The spectra were collected with a constant analyzer pass energy of 50 eV and with step sizes of 0.025 eV. The uncertainty in binding energy positions was determined by referencing the bulk gold Au $4f_{7/2}$ photoelectron line at 84.0 eV and a C 1s photoelectron line at 284.8 eV and estimated to be $\pm$0.02 eV. The as-obtained high-resolution Ag 3d core-level spectra were subject to a Shirley background subtraction followed by standard peak fitting procedures. These fitted values served as quantitative parameters for further analysis. The SERS measurements were carried out on a Micro Raman Identify Dual system (MRID-Raman, Protrustech Co., Ltd, Taiwan) mounted with one TE cooled CCD of 1024 × 256 pixels as integrated by Protrustech Corporation Limited. A 50 × long-working-distance lens (Olympus America, Inc.) was used to acquire SERS spectra at different laser excitation sources, with wavelengths of 532, 633, and 785 nm. Selected target molecules, BSA and SARS-CoV-2 (COVID-19) spike RBD protein, His tag (active) (Cat. No. GTX136090), and SARS-CoV/SARS-CoV-2 (COVID-19) spike antibody [1A9] (Cat. No. GTX632604) from GeneTex co., were used for SERS measurements. Spectra were acquired from at least ten different points on one sample with a constant integration time of 5 s for all SERS measurements. The as-obtained spectral data were preprocessed with the asymmetric least squares method for baseline correction and

then averaged to obtain the final spectrum, which was used for quantification purpose.

III. RESULTS AND DISCUSSION

A. Characterization of the synthesized silver nanowires

The polyol method is one of the most widely employed wet chemical approach-based synthesis methods for synthesizing anisotropic metal nanostructures.[32] Typically, a metal precursor (silver nitrate, $AgNO_3$, in our case) is dissolved in a polyol (ethylene glycol, EG, in our case) in the presence of a suitable capping agent (polyvinylpyrrolidone, PVP, in our case). Varying the available parameters, such as temperature, rate of addition, molar ratio between the constituents, and reaction time, can result in a variety of nanostructured products with different morphologies. The detailed preparation is described in the ESI.

Morphological and structural characterization was performed by scanning electron microscopy (SEM), x-ray diffraction (XRD), and dynamic light scattering (DLS), respectively (Fig. S1). The as-synthesized silver nanowire solution was sprayed onto a clean silicon substrate and vacuum dried. Figure S1(a) shows the morphology of our as-synthesized silver nanowires (AgNWs). The broad plasmon resonance spanning the entire visible range of the AgNWs is evident in Fig. S1(b). The x-ray diffraction (XRD) patterns of the AgNWs, indexed according to JCPDS card no. 04–0783 of cubic silver, are shown in Fig. S1(c). The patterns revealed major peaks (2θ) at 38.12, 44.42, 64.41, 77.53, and 81.59 A°, corresponding to the (111) (200), (220), (311), and (222) cubic silver crystal planes, respectively. The most intense peak at 38.12 A°, indicative of the (111) crystal plane, and the lattice parameter of 4.08 A° are both in good agreement with the results reported in the literature for silver nanowires.[36] Figures S1(d) and S1(e) present the average values for the diameter and length of the silver nanowires. Although there is a broad dispersion in size, characteristic values of (96.46 ± 27.84) nm in diameter and (3.13 ± 2.64) μm in length were collected by DLS. We extracted the size of nanowires from statistical analysis of several SEM images and found that they were 80–120 nm in width and >2 μm in length.

B. Intrinsic electromagnetic field simulations of silver nanowires

Nanowires exhibit higher-order modes compared to either nanoparticles or nanorods. This is due to larger dimensions relative to the incident illumination wavelength. For all silver nanowire dimensions, we varied the excitation wavelength over a wide range, from 200 to 1800 nm, and found that the E-fields generated from these nanowires spanned a wide range from the visible to near infrared region [Figs. 2(a) and 2(b)]. The corresponding peak maxima of the E-field generated from AgNWs with varied dimensions were observed to vary from 390 to 630 nm. Nonetheless, the E-fields generated from these nanowires covered the visible range, irrespective of their dimensions. By varying in the length of the nanowires (with a constant diameter of 100 nm) from 50 to 5000 nm, we observed the electromagnetic magnitudes increased with increasing length but became saturated at approximately 4000 nm [inset in Fig. 2(b)]. Moreover, the silver nanowire diameter was varied at a constant length of 5000 nm [Figs. 2(c) and 2(d)]. With an initial increase from 50 to 100 nm, an increasing trend in the field magnitude was observed. A further increase in the diameter led to a decrease in the electromagnetic field [inset in Fig. 2(d)], thereby demonstrating the existence of an optimum value. The propagation of electromagnetic waves shown in actual aspect scale of nanowire is shown in Fig. S2. Here, we observed that the number of nodes

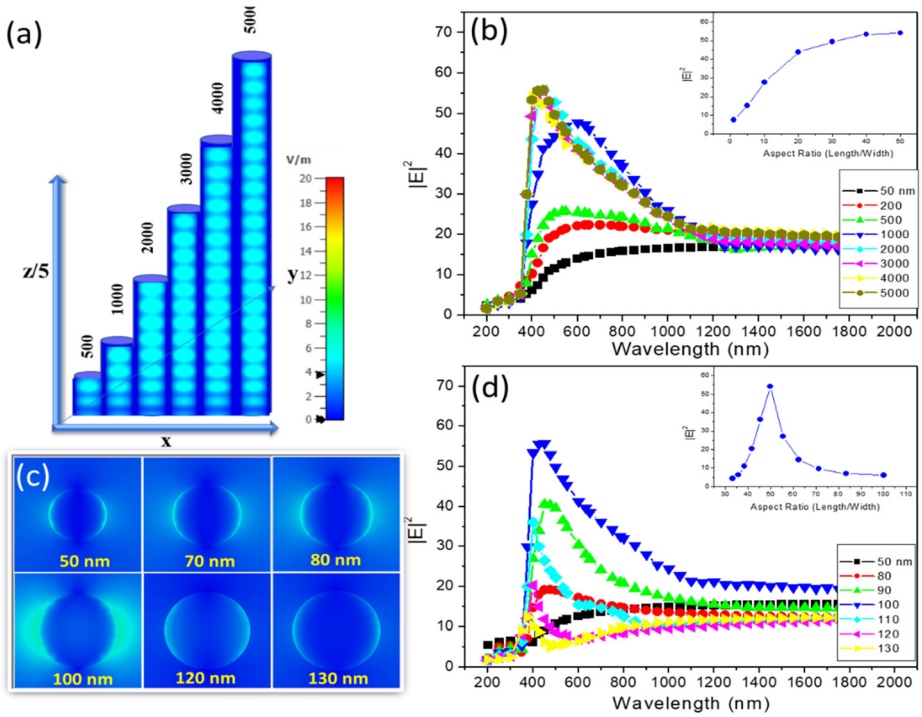

FIG. 2. Finite integral technique (FIT) simulations of AgNWs with varied dimensions used to construct multilayered 3D SERS substrates. Variations in the length of the nanowires with a constant diameter (100 nm) led to an increase in the E-field enhancement (a) and (b), which plateaued after reaching 3000 nm [inset in (b)]. Variations in the diameter of a 5000 nm-constant-length silver nanowire, resulted in an increase in E-field magnitudes with increasing diameter up to a certain extent (c) and (d), 100 nm, at which point this trend reversed [inset in (d)].

of the electromagnetic field is proportional to the length of the nanowire [Fig. S3(a)] and the energy of the incident light [Fig. S3(b)]. From these two different behaviors mentioned above, it can be concluded that the aspect ratio of the AgNWs strongly dictates the enhanced field behavior from an "individual silver nanowire." In addition, irrespective of the variations in the length or diameter of the AgNWs, the EM fields in all cases spanned the entire visible range, characteristic of anisotropic AgNWs.

C. Electromagnetic field simulations of possible plasmon coupling between two silver nanowires

Next, simulations were carried out to investigate the gap-dependent E-field enhancements between two nanowires. The maximum E-fields from a two-parallel-nanowire system as a function of the interwire gap distance are shown in Fig. 3(a). It was observed that the magnitudes of the field enhancements decreased very rapidly with increasing distance, indicating a significant reduction in the plasmon coupling between the two parallel nanowires, which was least-square-fitted to demonstrate that the decay could be approximated by a double-decay exponential function [equation inserted in Fig. 3(b)]. Then, we considered a simulation with an alternative arrangement geometry of two nanowires, end-to-end, for the scaling of the E-field enhancement. It is known that mimicked metal–insulator (media)–metal (MIM) systems have demonstrated near-perfect optical absorption, immense radiative rate enhancements, and independent tunability of the spectral response and modal intensity.[37] Figure 3(c) shows the distance-dependent field decay between two end-to-end nanowires. Although the maximum E-field in this case is not as intense compared to the that of parallel mode in Fig. 3(a), this mode is typically nonnegligible, symmetric, and tightly localized in the nanogap region [zoom-in in Fig. 3(c)], which allows the enhanced optical processes to be tuned by varying the dielectric medium. Both of these results shown in Fig. 3 indicate that the E-field-enhanced phenomenon remains valid for nanowires, while greatly approximated exponential decays with the nanogaps increase. Moreover, the E-fields generated in these two geometries, parallel and end-to-end configurations, were also simulated under different laser excitation sources, i.e., 785, 633, and 532 nm, and demonstrated similar double-exponential decay behaviors [Figs. 3(b) and 3(d)]. The E-field magnitudes calculated at different laser-excited wavelength sources showed similar double-exponential decay behavior with respect to the distance of separation irrespective of configurations but with different magnitudes of intensities. The E-field in the end-to-end geometry is lower than that of parallel nanowires at all excited wavelength sources.

Investigating the multilayer packing, the interaction between two nanowires should be considered first. In addition to parallel and end-to-end alignment, it is highly probable that nanowires often intersect each other and thereby affect electromagnetic enhancement [Fig. 4(a)]. Here, we found that surface plasmons from nanowires can be tuned in the presence of another nanowire. This intersecting geometrical configuration of nanowires also yields an appreciable amount of E-field, which can result in SERS enhancement due to strong plasmon coupling. Furthermore, we also explored the E-field caused by stacking with different crossing angles, as shown, in Fig. S4. Surprisingly, the 40°–50° crossing produced a larger-amplitude plasmonic resonance oscillation, but the intensity is higher than that of 90°. Nevertheless, we summed and compared the E-fields caused by the above possible stacks. Figure 4(b) shows that a single nanowire also possesses propagating surface plasmons but has the lowest E-field in all configurations. Additionally, the area of influence of the E-fields is the largest in the case of two intersecting nanowires [hotspot indicated in Fig. 4(c)], which improves SERS enhancement by several factors compared to that in the case of other geometries. Combined with the results shown in Fig. 3, this demonstrates the importance of the nano-assembly, which plays a vital role in dictating the overall E-field. On the other hand, E-field distributions in all the cases, with respect to excitation laser sources of wavelengths 785, 633, and 532 nm, were also examined. Figure S4 also showed that higher wavelength (lower energy) light sources presented higher plasmonic resonance effects in all stacking conditions.

D. Construction of an M3D-SERS substrate and characterization with bovine serum albumin (BSA)

The scheme in Fig. 1 shows the procedure of using silver nanowires to fabricate an M3D-SERS substrate with random, crossed-wire,

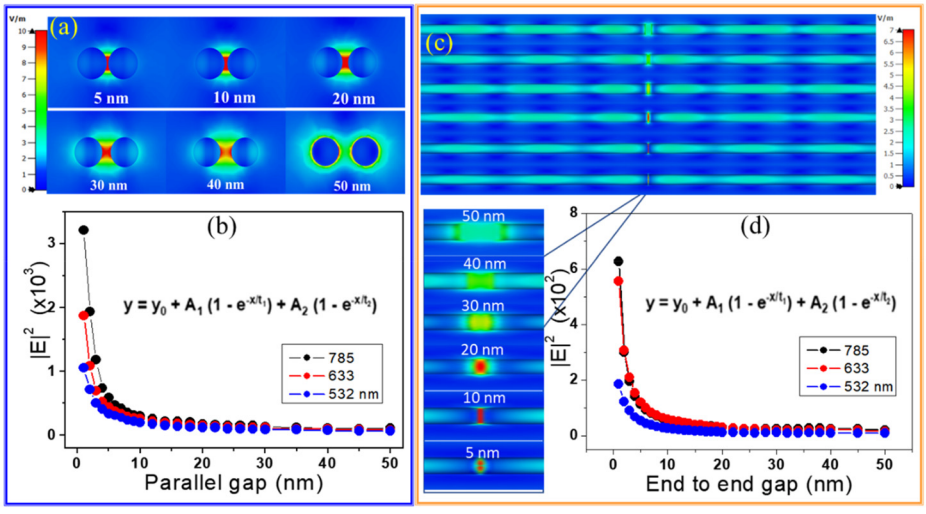

FIG. 3. Plasmonic hotspot generation and calculated E-fields with distance in two configurations: aligned or parallel nanowires (a) and (b) and end-to-end configurations (c) and (d).

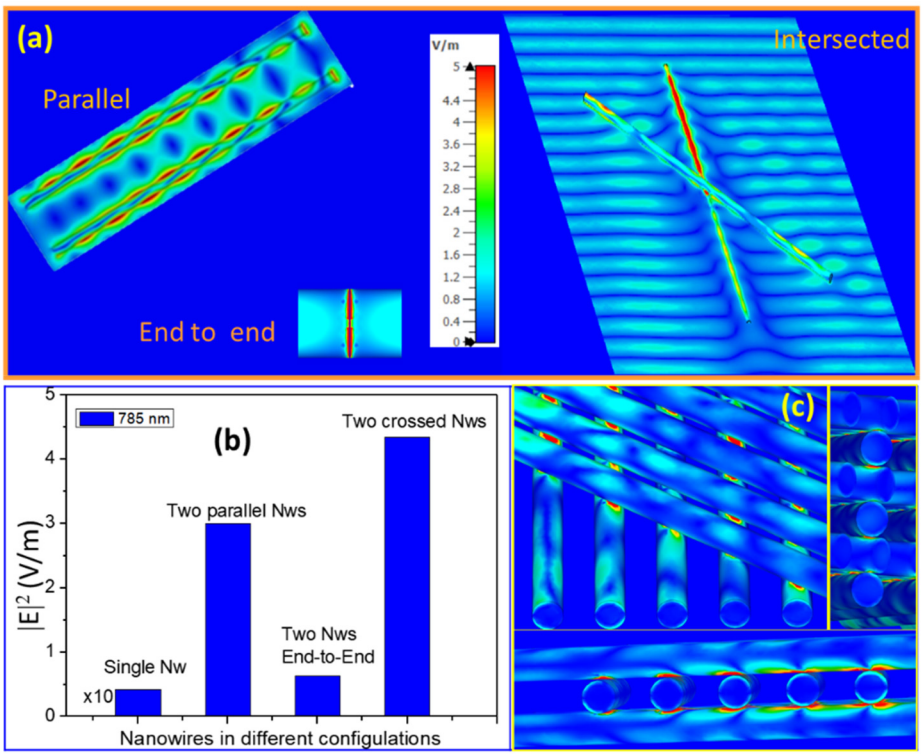

FIG. 4. (a) The possible interaction modes between two nanowires are parallel, end to end, and intersected. (b) The resulting E-field comparison in relation to the excitation energy. (c) Schematic diagram of hotspot formation from nanowires stacking under 785 nm excitation.

layer-by-layer packing through a very conventional sprinkling method. In this way, the layer number (along the z direction) and the density within the layer are determined according to how many volumes of nanowire-containing stock solution are sprayed into the well. The SEM surface morphologies of M3D-SERS substrates with increased Ag nanostructured layers, 1 L–6 L, are shown in Fig. 5(a). From x-ray photoelectron spectroscopic (XPS) analysis on Ag 3d core energy levels from all our SERS substrates with different layers, 1 L–6 L, we observe the two characteristic, Ag $3d_{5/2}$ and Ag $3d_{3/2}$ peaks [Fig. 5(b)]. The Ag $3d_{5/2}$ binding energy position occurs at 368.3 eV, consistent with reported values.[38] The spin–orbit-splitting values between the two core-level peaks remain constant at 6.0 eV, which is consistent with reported values. A qualitative overview shows that both the peak intensities increase with increase in the number of sprayed silver multilayers. To verify it quantitatively, we plotted the area under the Ag $3d_{5/-2}$ peak against the increasing multilayers. The resulting dependency was best fitted with the function

$$Y = Y_0 + A^* e^{(X/t)}. \quad (1)$$

Overall, x-ray photoelectron spectroscopic (XPS) analysis revealed the multilayer dependent features from our as-constructed SERS substrates.

After drying, the SERS characteristics of the M3D-SERS chips were examined based on bovine serum albumin (BSA) to evaluate the optimized layer packing and AgNW gathering density. The SERS results from BSA with an excitation wavelength of 633 nm on the M3D-SERS substrate included peaks at ~845, 1008, 1139, 1241, 1401, and 1593 cm^{-1} [Fig. 6(a)], which match those reported in the literature.[39] Moreover, the spectral comparison of M3D-SERS chips of variable densities indicated that the intensity of the Raman spectra apparently increased up to the fourth cycle (4 L) of AgNW sprinkling [experiment 2.2, Fig. 1(a)] with a constant concentration of BSA (10 nM × 10 μL). The high SERS signal enhancement can be explained by the fact that more layer formation, more cross-stacked nanowires, and more z-direction hotspots inside the M3D-SERS eventually induced strong plasmonic coupling along the vertical direction [Fig. 1(b)].[40,41]

On the other hand, the signal intensity decreased with more than four cycles of spreading, which can be explained by the fact that the transmittance of the substrate decreases dramatically as the number of stacking layers increases and then causes the incident light (and the Raman signal output) penetration to decrease. Moreover, if the molecules are distributed in more layers, the number of molecules in each layer decreases. Nevertheless, transmittance is the criterion for fabricating an optimized M3D-SERS substrate for SERS measurement. Furthermore, light source-dependent SERS spectra were collected using 532, 633, and 785 nm excitation, as shown in Fig. 6(b). We observed the same Raman bands in the relative spectral range, while there was variation in the relative intensities. The variation in the Raman spectra from a single location acquired using different excitation wavelengths revealed the coupling between the phonons and electronic transitions. During the experiment, we found that strong excitation energy is easy to damage biological organic molecules, whether it is stronger laser energy, longer exposure time, or more times of CCD accumulation. Consequently, we concluded that lower energy excitation was the most suitable for BSA biomolecule SERS measurement, and the LOD (limit of detection) was approximately 10 pM [Figs. 6(c) and S5]. Finally, the minimum detection limit for BSA was determined to be 10^{-11} M in 10 μL volumes using a M3D-SERS (4 L) chip.

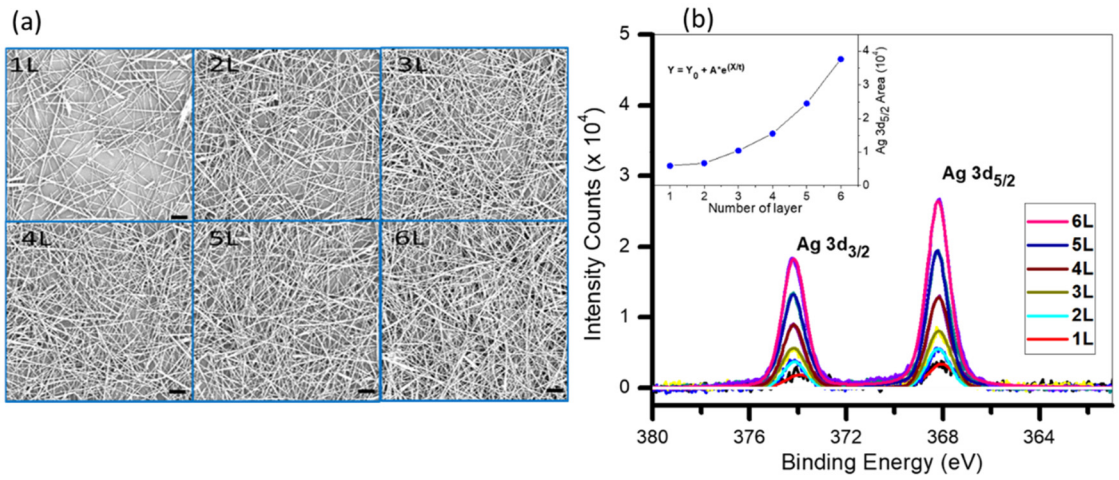

FIG. 5. (a) The relative scanning electron micrographs (SEMs) and (b) Ag 3d x-ray photoelectron spectroscopic (XPS) analysis from M3D-SERS substrates for 1 L–6 L. Inset in (b) shows a quantitative analysis of the area under the peak-fitted Ag $3d_{5/2}$ component.

Here, we tested the uniformity and reproducibility of M3D-SERS substrates. At first, we also constructed the M3D-SERS substrate by adding the entire AgNWs directly (not step-by-step procedure, as Fig. 1 shown) onto the glass substrate and then following the same vacuum drying process. We used 10 nM of BSA as a probe molecule to see the difference in the SERS spectra. Here, SERS spectra were collected from ten different positions of substrate, and Fig. S6(a) presents that the one-time layer packing approach provides higher SERS signal data with reproducible repeatability with a data error distribution <15%, while layer-by-layer case reveals slightly lower signal, but better consistency with a data error distribution <10%, as can be seen from Fig. S6(b). In light of these findings, we have emphasized on the greater uniformity from the multilayered nanostructured substrates, leading to the generation and propagation of plasmonic modes not only on the xy plane but also in the z direction. This three-dimensional plasmonic behavior adds another dimension to the understanding of the SERS

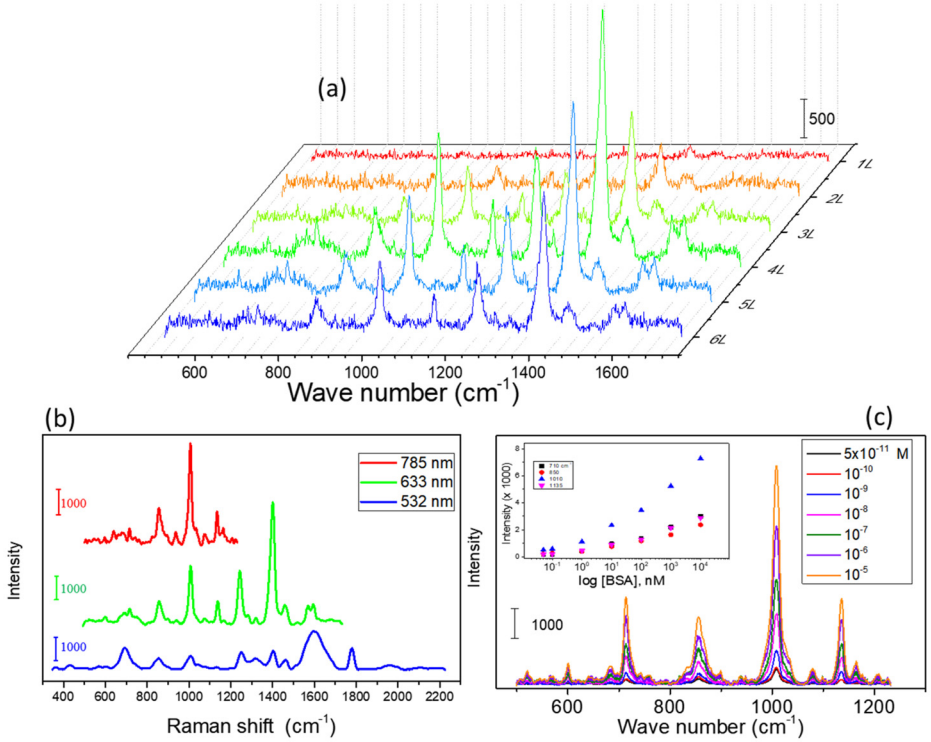

FIG. 6. Surface-enhanced Raman spectra for BSA biomolecule on the prepared substrate: (a) 10 μL of 10 nM BSA sprinkled onto glass coating with Ag NWs of variable densities (10 μL × 1, 2, 3, 4, 5, 6, respectively). (b) Laser light source-dependent (532, 633, 785 nm) SERS spectra of 0.1 μM BSA. (c) SERS detection limit for BSA using a 785 nm laser. 10 μL of analyte was used to collect the SERS spectra.

enhancement mechanisms. Furthermore, another reproducibility for M3D-SERS substrates was tested after the prepared chip was placed in the atmosphere for over 90 days. The SERS signal could still be detected with a decrease in less than 10%, as shown in Fig. S7.

E. SARS-CoV-2-related biomolecules (antigen/antibodies)

With the current ongoing SARS-CoV-2 pandemic, which is caused by a virus that is highly contagious and fast-transmitting in nature,[42] we recommend detecting SARS-CoV-2-related biomolecules (antigens/antibodies) by using SERS technology, primarily owing to its nondestructive nature, ease of sample preparation, and capability to facilitate detection at a distance in ambient environmental conditions. Figures 7 and S8 show the SERS spectra collected from spike RBD protein (S-protein) and its antibody (1A9-protein) by M3D-SERS. To determine the manufacturing conditions for the mass production of M3D-SERS to achieve fast screening, the number of AgNW layers was varied from a single layer (1 L) to six layers (6 L). As can be observed, the largest SERS enhancements of S-protein and 1A9-protein (10 nM) were obtained with the M3D-SERS substrate with ~four layers (4 L) of AgNWs, at all three excitation wavelengths of laser sources. The enhanced SERS responses from the different vibrational bands were also observed to be layer dependent. As expected, similar to the situation encountered by BSA, the well-resolved Raman peaks were not observed at 532 nm condition (Fig. 8). There are some spectral broadenings around 1400 and 1600 cm^{-1}, implying the decomposition of organic molecules. We will not discuss it further in this manuscript. On the other hand, since sensitivity is a key factor in SERS, a nanomolar concentration of each biomolecule was used to test the efficiency of the multilayer M3D-SERS under different excitation sources, which is shown in Fig. 7. Therefore, we concluded that M3D-SERS can detect biomolecules (both S-protein and 1A9-protein) at a level of 0.1 nM, no matter under the laser conditions of 633 or 785 nm (Fig. S9).

Distinct Raman peaks from S-protein and 1A9-protein were peaked and assigned as shown in Fig. 8(a). With the SERS of SARS-CoV-2 being a recent observation, both the processes of resolving the technical difficulties of its detection and peak assignment, the observed vibrational bands based on rigorous theoretical calculations are being continuously refined and developed. We assigned these vibrational peaks based on the corresponding results reported in the available literature.[43–48] There is no doubt that these signals we obtained indicate the secondary structure of a bioorganic molecule.[49] However, we found that the Raman signals in these journal articles are weak, and even need to use statistics programs to amplify the data (signals) for differentiating variable biomolecules. In contrast, the Raman spectra in Fig. 7 are intense, clear, and well-defined. More importantly, we find out the corresponding excitation laser light source to avoid the problem that the biomolecule is easy to decompose. Therefore, we do not need program statistics to amplify data, and we do not need to use reporter to indirectly show the detection limit of SARS-CoV-2 and emphasize the convenience of detection. For example, using Fig. 8, we can easily compare the difference in Raman signal between the spike protein and its antibody. We can observe that lasering 633 nm seems to be able to get well-defined spectra and excellent detection limit between three excitation light sources, while the SERS spectra in 785 nm can reveal a more obvious difference between spike and antibody [Fig. 8(b)]. Here, we found that the signal difference between 1A9 antibody and spike antigen may mainly come from the difference in Trp number [737, 887, 1579 cm^{-1} in Fig. 8(a)] and accompanied by a little difference in secondary structure (α-helix, 1646, 1288 cm^{-1}).

On the other hand, it is very important whether this platform can recognize antibodies in the presence of other biomolecules or in the blood environment. As mentioned in this manuscript, as long as we can detect the SERS signal, we can get the Raman fingerprint for identification. Figure S10 shows the results of variable mixing ratios of antibody 1A9 in HSA. It can be seen that our platform can still recognize the signal of the antibody. Meanwhile, we have also made a comparative analysis with different SERS substrates, other detection methods,

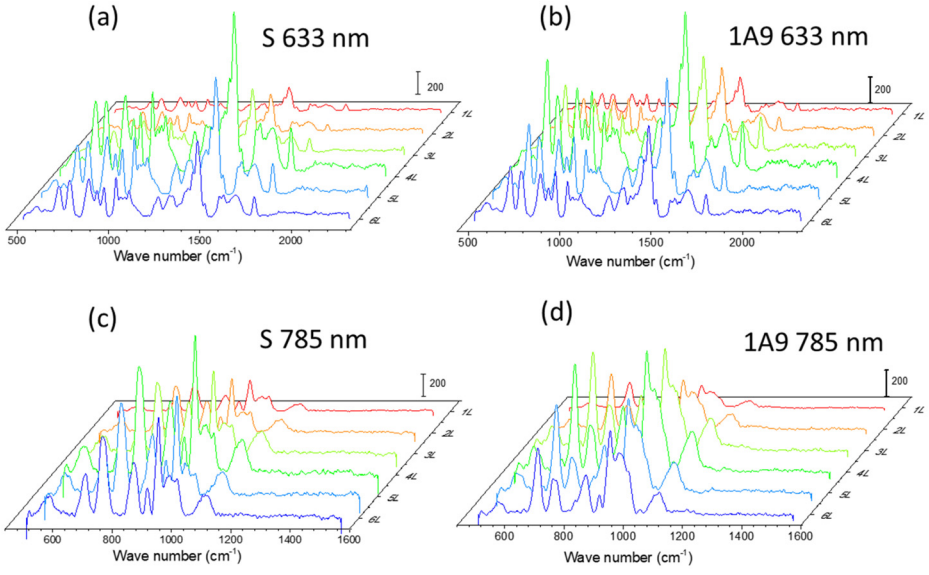

FIG. 7. Surface-enhanced Raman spectra of 10 μL of 10 nM spike-protein (a) and (c) and 1A9-protein (b) and (d) biomolecules sprinkled onto glass coating with Ag NWs of variable densities (20 μL × 1, 2, 3, 4, 5, 6, respectively). Laser light source-dependent 532 nm (Fig. S5), 633 nm (a) and (b), 785 nm (c) and (d).

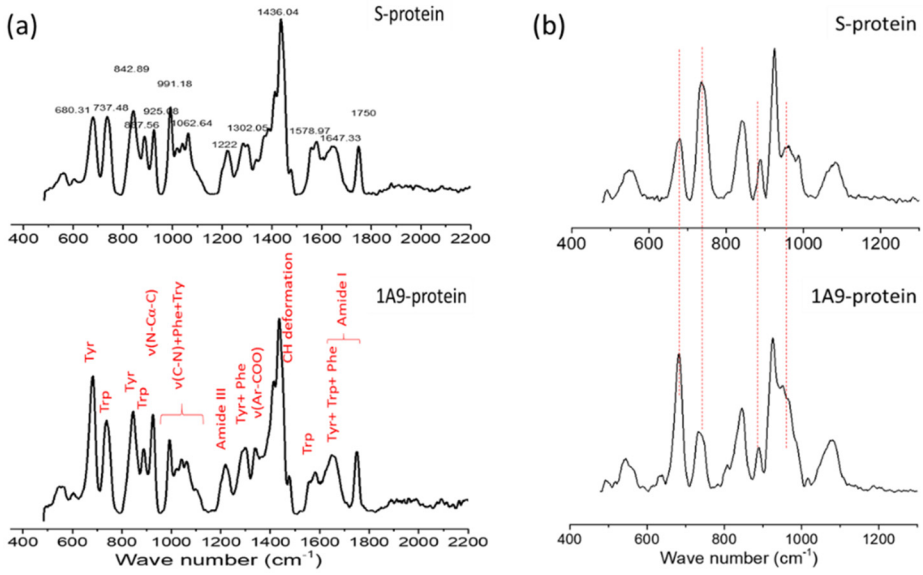

FIG. 8. Distinct Raman peaks from S-protein and 1A9-protein are assigned to compare the differences in (a) 633 nm and (b) 785 nm spectra.

materials, and limit of detection values from the target analytes. Our approach leverages a single-component nanostructure, offers label-free detection, and does not require the use of advanced statistics or machine learning algorithms for data analysis to achieve sensitive and accurate detection of BSA (Table S1) and SARS-CoV-2 biomolecules (Table S2 in ESI). The integration of these features within our research framework aims to uncovering the intricate interactions between biomolecules in different biological environments.

F. A comparative analysis of experimental and theoretical simulation results

To understand such unique features, it is necessary to perform a systematic study to model AgNWs and simulate them to calculate the E-fields in terms of layer-dependent E^2 with different AgNW layers and different excitation wavelength sources. Simulations were performed on the AgNWs with the dimensions of 5 μm (length) $\times$ 100 nm (diameter) as input parameters. Followed the condition and parameter in Figs. 2 and 3, simulation was carried out on each individual 2D AgNW layer in the 3D multilayered substrate to investigate in-depth the behavior and magnitudes of the E-fields. (Fig. 9).

In the case of one-layered (1 L) AgNWs, the SERS enhancement solely originated from the nanowire gaps, in either aligned or end-to-end configurations, as Fig. 3 shown. It is different from that observed in the case of AgNWs with two layers (2 L) or more due to (1) the generation of nanogaps in the vertical (z-axial) direction and (2) interlocking nanowires. These three types (vertical and lateral nanogaps and intersecting nanowires) of hotspots were generated with the addition of each AgNW layer. This followed a sequence of consecutive assemblies of layers, initially beginning with a monolayer (1 L) or two-dimensional (2D) to a three-dimensional (3D) configuration of two layers (2 L). With such a transition from a 2D to a 3D AgNW assembly, the increased number of intersections resulted in a significant increase in the number of SERS hotspots. That is, an increase in the number of layers of course increased the probability of nanowire intersection [hotspot, Fig. 9(b)]. In this way, the entire M3D-SERS chip underwent *homogeneous plasmonic coupling* [Fig. 1(b)] and it was obvious that hotspots were dominant and the most important factor. Therefore, the collective plasmonic coupling in the directions of the x–y (parallel gap) and x–z (perpendicular gap) axes must be effectively exploited to design large-area, uniform, and ultrasensitive SERS platforms.

A multilayer 3D-SERS substrate has an exposed top outermost layer for target molecules as well as photons from the laser source to interact with, thus providing more access compared to the intermediate layers. That is, the intermediate layer provides in a comparatively lowered SERS performance, owing primarily to the restricted plasmonic area. Thus, the overall utilization efficiency of the substrate is lowered. In addition, the increase in space height due to these vertically stacked 2D interlayers imposes a threshold on the penetration depth of each individual laser beam, thereby limiting the SERS performance from the multilayered 3D-SERS substrates. That is why the M3D-SERS exhibits an optimal layer (L = ~4) packing condition [Fig. 9(c)].

For all biomolecules (HSA, S-protein, 1A9), we plotted the strong and intense Raman peak intensities from the analyzed biomolecules placed on the M3D-SERS substrates. Initially, the SERS intensities increased with an increasing number of 2D AgNW interlayers and plateaued after reaching their maxima at 3–4 layers [Fig. 9(d)]. The lower SERS enhancement from a single AgNW layer (1 L) could be due to the presence of insufficient number of hotspots. This is because there is less interlocking of nanowires, as well as an increased distance between two adjacent nanowires. As a result, one should expect a lower E-field enhancement in the initial layer. Compared to that of the first layer, an increased SERS response from additional AgNW layers toward the target molecules is reasonable. The addition of a subsequent layer resulted in a decrease in the nanogaps and an increase in the intersection. More importantly, an additional factor was that the analyte molecule was trapped in a three-dimensional field filled with plasmonic enhancements. On the other hand, the increasing trend of the SERS intensities reversed with a further increase in the number of

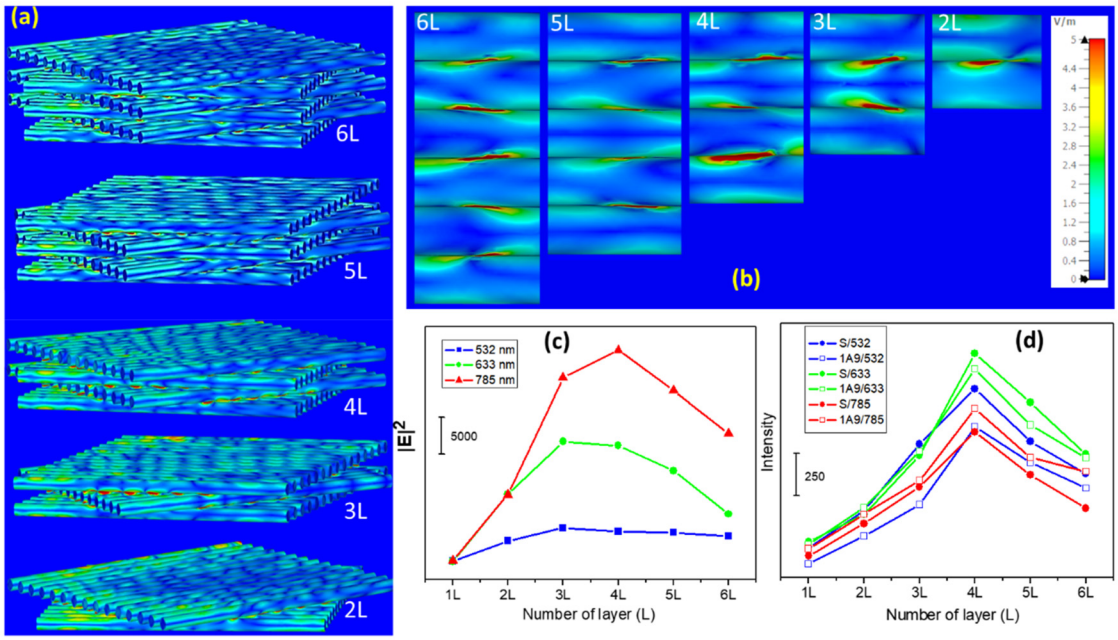

FIG. 9. Simulation results of layer-dependent 3D AgNWs (a) and their relative z-direction hotspot formation (b). Comparison between theoretical E-field values and experimental SERS results of the multilayer nanostructured AgNWs: FIT-simulated E-field values show the existence of an optimum irrespective of incident irradiation wavelength sources (c), which is also well supported by the experimental SERS measurements of 2D AgNW layers with different biomolecules under the same conditions (d).

2D AgNW layers, which can be explained by the increasing close-packed structures of the multilayers with depth drastically influencing the finite penetration depth of the laser excitation source. Therefore, signals that would have provided information on the deeply buried layers were either blocked or scattered between the layers, thereby resulting in weaker SERS signals.

The results above indicated that each increasing layer had an impact on the overall E-field from the substrate. Both the SERS and FIT results further confirmed the previous results. Figures 9(c) and 9(d) show that the simulated trend of the electric field between different layers was similar to the trend of the Raman peak intensity obtained from the experiment, even at different excitation wavelengths of 785, 633, and 532 nm. This confirmed that the 3D plasmons, both in the x–y and x–z directions, nanogaps, and the distance between them were the major contributing factors toward such SERS enhancement from a relatively simple, single-component SERS substrate. Based on the above results, we propose a simple, single-component, multilayer-structured M3D-SERS substrate fabricated from silver nanowires. This kind of substrate with layer-by-layer 3D packing generates intense E-fields along the vertical and parallel nanogaps, thus resulting in a high density and isotropic plasmon coupling inside the substrate. Furthermore, the interlocking of AgNWs forms a homogeneous 3D hotspot distribution compared to the loosely packed 2D monolayer nanostructures. The SERS enhancement is much higher in a multiscale assembly of 4 ± 1 layers, thereby indicating that a thin SERS substrate from only one component (e.g., Ag) can purposefully result in a highly sensitive SERS substrate. Most of the related reports are based on 1D or 2D assembled SERS substrates. Our study could thus fill this knowledge gap and provide a better understanding of 3D SERS substrates.

Finally, we need to discuss about the morphological discrepancy between the experimentally obtained constructs and the models for FIT simulations. In this ideal case, if the nanowires are perfectly aligned and crossed, we can control and predict the hotspots and quantify the generated electric fields with high precision. On the other hand, in practical scenarios, more interactions are possible from a vast array of geometric configurations, such as angles, overlaps, or distances. The collective response may lead to the generation of extra hotspots and expected electric fields of greater strength. In Fig. 4, we have shown that, for two silver nanowires, AgNWs in aligned or end-to-end configurations can also generate higher electromagnetic fields, albeit at lower strengths compared to crossing nanowires. Moreover, the result of Fig. S4 further proved that the orthogonal interaction is not the best result. Therefore, it can be inferred that the effect of the M3D-SERS substrate will be better than the theoretical calculation.

Another important issue for the construction of random-crossed stacking AgNWs in M3D-SERS substrate is the applicability to the analytes, although many kinds of the literature reported their special technologies to fabricate oriented layer-by-layer silver nanowires with a relatively precise arrangement, resulting in an organized structure. The regular orthogonal stacking can only allow a specific size of the analyte to be deposited. While it is different in M3D-SERS substrate, we want to construct a randomly arrange nanowires and stack them layer by layer to create variable sizes of defects, so as to "trapped" the variable sizes analytes, which can be surrounded by plasma coupling region. That is why we used a spraying process to construct a randomly cross-stacked M3D-SERS substrate and expect it to successfully detect variable size of analytes (small organic molecules, DNA, protein, and virus).

IV. CONCLUSION

In summary, we developed an M3D-SERS chip suitable for detecting biomolecules by fabricating an ultrasensitive, multi-layered, 3D, single-component SERS substrate from silver nanowires via a consecutive layer-by-layer assembly method. Using finite integration technique (FIT) simulations with specific emphasis on the addition of individual AgNWs under different laser excitation sources revealed that the extremely localized plasmonic hotspots in the vertical and lateral directions from the nanogaps were responsible for SERS enhancement from the M3D-SERS substrate. Experimentally, the M3D-SERS substrate demonstrated a nanomolar-concentration detection level for three different types of biomolecules: bovine serum albumin and SARS-CoV-2 antigen and antibody. Three different laser sources also further demonstrated similar detection levels. Both the experimental and theoretical simulation results excellently corresponded with each other and indicated the existence of an optimum limit of the 2D layer in the 3D SERS substrate, which is responsible for the highest SERS enhancement. This simple approach of fabricating a single-component, multi-layered, 3D SERS substrate has application potential in the clinical diagnosis of different biomolecules.

SUPPLEMENTARY MATERIAL

See the electronic supplementary material for synthesis detail and characterization of the nanowire and for Figs. S1–S10 and Tables S1 and S2.

ACKNOWLEDGMENTS

This research was supported by the Ministry of Science and Technology (No. MOST 111-2113-M-005-x2013;013-), (No. MOST 110-2221-E-005-049-MY2), and (No. MOST359-2634-F-005 -001-) of Taiwan.

This work was also financially supported (in part) by the Advanced Plant Biotechnology Center from The Featured Areas Research Center Program within the framework of the Higher Education Sprout Project by the Ministry of Education (MOE) in Taiwan.

AUTHOR DECLARATIONS

Conflict of Interest

The authors have no conflicts to disclose.

Author Contributions

S.R.S. performed the theoretical simulations.

Smruti R. Sahoo: Data curation (lead); Formal analysis (equal); Investigation (equal); Writing – original draft (equal). **Chun-Ta Huang:** Conceptualization (lead); Investigation (equal); Resources (equal). **Kunju Tsai:** Resources (equal). **Gou-Jen Wang:** Conceptualization (equal); Investigation (equal); Supervision (equal). **Cheng-Chung Chang:** Conceptualization (equal); Data curation (equal); Project administration (equal); Writing – original draft (equal).

DATA AVAILABILITY

The data that support the findings of this study are available from the corresponding authors upon reasonable request.

REFERENCES

[1]Y. Huang, Y. Fang, Z. Zhang, L. Zhu, and M. Sun, "Nanowire-supported plasmonic waveguide for remote excitation of surface-enhanced Raman scattering," Light Sci. Appl. **3**, e199 (2014).
[2]E. C. le Ru, M. Meyer, and P. G. Etchegoin, "Proof of single-molecule sensitivity in surface enhanced Raman scattering (SERS) by means of a two-analyte technique," J. Phys. Chem. B **110**, 1944 (2006).
[3]J. A. Dieringer, R. B. Lettan, K. A. Scheidt, and R. P. van Duyne, "A frequency domain existence proof of single-molecule surface-enhanced Raman spectroscopy," J. Am. Chem. Soc. **129**, 16249 (2007).
[4]M. Fleischmann, P. J. Hendra, and A. J. McQuillan, "Raman spectra of pyridine adsorbed at a silver electrode," Chem. Phys. Lett. **26**, 163 (1974).
[5]G. Habibullah, J. Viktorova, and T. Ruml, "Current strategies for noble metal nanoparticle synthesis," Nanoscale Res. Lett. **16**, 47 (2021).
[6]S. S. Panikar, D. Cialla-May, E. de la Rosa, P. Salas, and J. Popp, "Towards translation of surface-enhanced Raman spectroscopy (SERS) to clinical practice: Progress and trends," TrAC, Trends Anal. Chem. **134**, 116122 (2021).
[7]J. Langer *et al.*, "Present and future of surface-enhanced Raman scattering," ACS Nano **14**, 28 (2020).
[8]H. Wei, D. Pan, S. Zhang, Z. Li, Q. Li, N. Liu, W. Wang, and H. Xu, "Plasmon waveguiding in nanowires," Chem. Rev. **118**, 2882 (2018).
[9]X. X. Han, R. S. Rodriguez, C. L. Haynes, Y. Ozaki, and B. Zhao, "Surface-enhanced Raman spectroscopy," Nat. Rev. Methods Primers **1**, 87 (2021).
[10]M. Girmatsion, A. Mahmud, B. Abraha, Y. Xie, Y. Cheng, H. Yu, W. Yao, Y. Guo, and H. Qian, "Rapid detection of antibiotic residues in animal products using surface-enhanced Raman spectroscopy: A review," Food Control **126**, 108019 (2021).
[11]E. Akanny, A. Bonhommé, F. Bessueille, S. Bourgeois, and C. Bordes, "Surface enhanced Raman spectroscopy for bacteria analysis: A review," Appl. Spectrosc. Rev. **56**, 380 (2021).
[12]Y. Huang, W. Liu, Z. Gong, W. Wu, M. Fan, D. Wang, and A. G. Brolo, "Detection of buried explosives using a surface-enhanced Raman scattering (SERS) substrate tailored for miniaturized spectrometers," ACS Sens. **5**, 2933 (2020).
[13]M. Hardy, L. Kelleher, P. de Carvalho Gomes, E. Buchan, H. O. M. Chu, and P. Goldberg Oppenheimer, "Methods in Raman spectroscopy for saliva studies—A review," Appl. Spectrosc. Rev. **57**, 177 (2022).
[14]C. G. Atkins, K. Buckley, M. W. Blades, and R. F. B. Turner, "Raman spectroscopy of blood and blood components," Appl. Spectrosc. **71**, 767 (2017).
[15]C. Zong, M. Xu, L. J. Xu, T. Wei, X. Ma, X. S. Zheng, R. Hu, and B. Ren, "Surface-enhanced Raman spectroscopy for bioanalysis: Reliability and challenges," Chem. Rev. **118**, 4946 (2018).
[16]A. Kozik *et al.*, "A review of surface-enhanced Raman spectroscopy in pathological processes," Anal. Chim. Acta **1187**, 338978 (2021).
[17]F. Hu, L. Shi, and W. Min, "Biological imaging of chemical bonds by stimulated Raman scattering microscopy," Nat. Methods **16**, 830 (2019).
[18]S. R. Sahoo, S. Huey-Jen Hsu, D. A. Chou, G. J. Wang, and C. C. Chang, "Surface plasmon-enhanced fluorescence and surface-enhanced Raman scattering dual-readout chip constructed with silver nanowires: Label-free clinical detection of direct-bilirubin," Biosens. Bioelectron. **213**, 114440 (2022).
[19]X. Pan, L. Bai, C. Pan, Z. Liu, and S. Ramakrishna, "Design, fabrication and applications of electrospun nanofiber-based surface-enhanced Raman spectroscopy substrate," Crit. Rev. Anal. Chem. **53**, 289 (2021).
[20]S. Das, L. P. Goswami, J. Gayathri, S. Tiwari, K. Saxena, and D. S. Mehta, "Fabrication of low cost highly structured silver capped aluminium nanorods as SERS substrate for the detection of biological pathogens," Nanotechnology **32**, 495301 (2021).
[21]X. Xue *et al.*, "Facile fabrication of PS/Cu_2S/Ag sandwich structure as SERS substrate for ultra-sensitive detection," Spectrochim. Acta, Part A **265**, 120370 (2022).
[22]Z. Q. Geng *et al.*, "Sensitive label-free detection of bilirubin in blood using boron nitride-modified nanorod arrays as SERS substrates," Sens. Actuators, B **334**, 129634 (2021).
[23]Z. Xie, F. Zhao, S. Zou, F. Zhu, Z. Zhang, and W. Wang, "TiO_2 nanorod arrays decorated with Au nanoparticles as sensitive and recyclable SERS substrates," J. Alloys Compd. **861**, 157999 (2021).

[24]W. Liao, K. Liu, Y. Chen, J. Hu, and Y. Gan, "Au–Ag bimetallic nanoparticles decorated silicon nanowires with fixed and dynamic hot spots for ultrasensitive 3D SERS sensing," J. Alloys Compd. **868**, 159136 (2021).
[25]S. Huang, C. Wu, Y. Wang, X. Yang, R. Yuan, and Y. Chai, "Ag/TiO_2 nanocomposites as a novel SERS substrate for construction of sensitive biosensor," Sens. Actuators, B **339**, 129843 (2021).
[26]I. Korkmaz *et al.*, "Fabrication of superhydrophobic Ag@ZnO@Bi_2WO_6 membrane disc as flexible and photocatalytic active reusable SERS substrate," J. Mol. Struct. **1223**, 129258 (2021).
[27]N. S. Mueller *et al.*, "Surface-enhanced Raman scattering and surface-enhanced infrared absorption by plasmon polaritons in three-dimensional nanoparticle supercrystals," ACS Nano **15**, 5523 (2021).
[28]B. G. M. Vieira, N. S. Mueller, E. B. Barros, and S. Reich, "Plasmonic properties of close-packed metallic nanoparticle mono- and bilayers," J. Phys. Chem. C **123**, 17951 (2019).
[29]F. Schulz, I. Lokteva, W. J. Parak, and F. Lehmkühler, "Recent notable approaches to study self-assembly of nanoparticles with x-ray scattering and electron microscopy," Part. Part. Syst. Charact. **38**, 2100087 (2021).
[30]F. Schulz *et al.*, "Plasmonic supercrystals with a layered structure studied by a combined TEM-SAXS-XCCA approach," Adv. Mater. Interfaces **7**, 2000919 (2020).
[31]Y. Zhou *et al.*, "High-performance flexible surface-enhanced Raman scattering substrate based on the particle-in-multiscale 3D structure," Nanophotonics **10**, 4045 (2021).
[32]C.-T. Huang, F.-J. Jan, and C.-C. Chang, "A 3D plasmonic crossed-wire nanostructure for surface-enhanced Raman scattering and plasmon-enhanced fluorescence detection," Molecules **26**, 281 (2021).
[33]H. Mao, J. Feng, X. Ma, C. Wu, and X. Zhao, "One-dimensional silver nanowires synthesized by self-seeding polyol process," J. Nanopart. Res. **14**, 887 (2012).
[34]T. Weiland, "Time domain electromagnetic field computation with finite difference methods," Int. J. Numer. Modell. Electron. Networks Devices Fields **9**, 295 (1996).
[35]P. B. Johnson and R. W. Christy, "Optical constants of the noble metals," Phys. Rev. B **6**, 4370 (1972).
[36]B. Bari *et al.*, "Simple hydrothermal synthesis of very-long and thin silver nanowires and their application in high quality transparent electrodes," J. Mater. Chem. A **4**, 11365 (2016).
[37]C. T. Chou Chao, Y. F. Chou Chau, and H. P. Chiang, "Highly sensitive metal-insulator-metal plasmonic refractive index sensor with a centrally coupled nanoring containing defects," J. Phys. D: Appl. Phys. **54**, 115301 (2021).
[38]A. Mosquera, J. Albella, V. Navarro, D. Bhattacharyya, and J. L. Endrino, "Effect of silver on the phase transition and wettability of titanium oxide films," Sci. Rep. **6**, 32171 (2016).
[39]M. G. Donato, V. P. Rajamanickam, A. Foti, P. G. Gucciardi, C. Liberale, and O. M. Maragò, "Optical force decoration of 3D microstructures with plasmonic particles," Opt. Lett. **43**, 5170 (2018).
[40]J. W. Jeong, M. M. P. Arnob, K.-M. Baek, S. Y. Lee, W.-C. Shih, and Y. S. Jung, "3D cross-point plasmonic nanoarchitectures containing dense and regular hot spots for surface-enhanced Raman spectroscopy analysis," Adv. Mater. **28**, 8695 (2016).
[41]X. Li, W. C. H. Choy, X. Ren, D. Zhang, and H. Lu, "Highly intensified surface enhanced Raman scattering by using monolayer graphene as the nanospacer of metal film-metal nanoparticle coupling system," Adv. Funct. Mater. **24**, 3114 (2014).
[42]J. Sitjar, J. der Liao, H. Lee, H. P. Tsai, J. R. Wang, and P. Y. Liu, "Challenges of SERS technology as a non-nucleic acid or -antigen detection method for SARS-CoV-2 virus and its variants," Biosens. Bioelectron. **181**, 113153 (2021).
[43]E. Zavyalova *et al.*, "SERS-based aptasensor for rapid quantitative detection of SARS-CoV-2," Nanomaterials **11**, 1394 (2021).
[44]M. Zhang *et al.*, "Ultrasensitive detection of SARS-CoV-2 spike protein in untreated saliva using SERS-based biosensor," Biosens. Bioelectron. **190**, 113421 (2021).
[45]G. Huang *et al.*, "Construction of optimal SERS hotspots based on capturing the spike receptor-binding domain (RBD) of SARS-CoV-2 for highly sensitive and specific detection by a fish model," Anal. Chem. **93**, 16086 (2021).
[46]C. Carlomagno *et al.*, "COVID-19 salivary Raman fingerprint: Innovative approach for the detection of current and past SARS-CoV-2 infections," Sci. Rep. **11**, 4943 (2021).
[47]Y. Yang *et al.*, "Human ACE2-functionalized gold "virus-trap" nanostructures for accurate capture of SARS-CoV-2 and single-virus SERS detection," Nano Micro Lett. **13**, 109 (2021).
[48]Y. Peng *et al.*, "Charge-transfer resonance and electromagnetic enhancement synergistically enabling MXenes with excellent SERS sensitivity for SARS-CoV-2 S protein detection," Nano Micro Lett. **13**, 52 (2021).
[49]A. Rygula *et al.*, "Raman spectroscopy of proteins: A review," J. Raman Spectrosc. **44**, 1061 (2013).